PAPER

Check for updates

Lateral heterostructures of monolayer group-IV monochalcogenides: band alignment and electronic properties†

Kai Cheng,[a] Yu Guo,[a] Nannan Han,[a] Yan Su,*[a] Junfeng Zhang[b] and Jijun Zhao [ID] *[ac]

Lateral semiconductor/semiconductor heterostructures made up of two-dimensional (2D) monolayer or few-layer materials provide new opportunities for 2D devices. Herein, we propose four lateral heterostructures constructed by phosphorene-like monolayer group-IV monochalcogenides, including GeS/GeSe, SnS/GeSe, SnSe/GeS and GeS/SnS. Using first-principles calculations, we investigated the energetics and electronic properties of these lateral heterostructures. The band structures and formation energies from supercell calculations demonstrate that these heterostructures retain semiconducting behavior and can be easily synthesized in the laboratory. The band offsets of monolayer, bilayer and trilayer heterojunctions at the Anderson limit are calculated from the valence/conduction band edges with respect to the vacuum energy level for each individual component. Among them, some heterostructures belong to type II band alignment and are promising for a high-efficiency solar cell.

Introduction

Semiconductor heterostructures of conventional three-dimensional (3D) materials have served as the most important aspect of electronic and optoelectronic device innovations over the last 50 years. The wave of two-dimensional (2D) materials research[1–3] motivates scientists to explore novel heterostructures based on 2D materials and to develop next-generation 2D devices with high performance.[4] Due to the reduced dimensionality, there are generally two possible types of 2D heterostructures. One is the vertical heterostructure, which can be achieved by layer-by-layer stacking with van der Waals (vdW) interactions.[5,6] The other is the lateral (in-plane) heterostructure, which can be obtained by stitching two semi-infinite layers into a shared platform with a one-dimensional (1D) interface.[7–16] Compared to the vertical

heterostructures, the lateral heterostructures have the advantages of simpler band alignment, a smaller interface region, and more distinct phase separation.[10] Moreover, the domains in a lateral heterostructure are usually connected by covalent bonds, ensuring the epitaxial quality and thus boosting the optical and electrical properties of the heterostructure.[15,17] All these virtues make lateral heterostructures rather competitive in practical applications.

To date, high-quality lateral 2D heterostructures have been synthesized in the laboratory. Several new phenomena have been found, and some prototype devices have been demonstrated. Specifically, lateral semiconductor/semiconductor (S/S) heterostructures based on transition metal dichalcogenides (TMD) monolayers,[7–9,18–20] including WS_2/MoS_2, $MoS_2/MoSe_2$, WS_2/WSe_2 and $MoSe_2/WSe_2$, have been fabricated in the past three years. These heterostructures exhibit strong localized photoluminescence[7,9] and p–n diode rectification characters,[7,8] showing perspectives in phototransistors and field-effect transistors. Using an advanced two-step epitaxial growth method, completely heterogeneous WSe_2/MoS_2 lateral heterostructures have been synthesized,[10] which also show an intrinsic p–n diodes feature. In addition, the band alignments of TMD-based lateral S/S heterostructures have been widely explored. Rivera's group[13] and Chiu's group[14] found type II band alignment in lateral $MoSe_2/WSe_2$ and MoS_2/WSe_2 heterojunctions that are useful for photovoltaics. On the other hand, Shih *et al.* found type I alignment in lateral bilayer-monolayer heterostructures based on $MoSe_2$ or WSe_2.[16] Some of these heterostructures can produce a light-induced exciton, which may find applications in laser,

a Key Laboratory of Materials Modification by Laser, Ion and Electron Beams (Dalian University of Technology), Ministry of Education, Dalian 116024, China. E-mail: su.yan@dlut.edu.cn, zhaojj@dlut.edu.cn

b School of Physics and Information Engineering, Shanxi Normal University, Linfen 041000, China

c Beijing Computational Science Research Center, Beijing 100094, China

† Electronic supplementary information (ESI) available: Band structures, total DOS and partial DOS, and charge density difference of individual (a) GeS, (b) GeSe, (c) SnS and (d) SnSe monolayers. Heat of formation (HF) for four monolayer lateral interfaces with different supercell lengths. Band structures of monolayer SnS/GeSe heterostructures with different widths. Partial charge distributions corresponding to the VBM and CBM for monolayer SnS/GeSe and SnSe/GeS heterostructures. Band-edge positions of isolated monolayer, bilayer and trilayer group-IV monochalcogenides relative to the vacuum level. CBO and VBO of monolayer, bilayer and trilayer SnS/GeSe heterostructures. See DOI: 10.1039/c7tc00595d

3788 | *J. Mater. Chem. C,* 2017, **5**, 3788–3795

This journal is © The Royal Society of Chemistry 2017

light emitting diodes and photovoltaic devices.[13] In addition, Strano et al. recently synthesized a monolayer WSe$_2$/MoS$_2$ lateral heterostructure that exhibits a selective switchable photoresponse.[15]

Parallel to the experimental efforts mentioned above, theoretical calculations using density functional theory (DFT) have been performed to explore the physical properties of lateral heterostructures. Kang et al. investigated the band structures and band offsets of lateral heterostructures based on MX$_2$ (M = Mo, W; X = S, Se, Te), and found that these heterostructures with type II band alignment are effective for the separation of the electron–hole pair and thus suitable for optoelectronics and energy conversion.[12] Later they investigated the possibility of tuning band alignment and charge localization in MoS$_2$/WS$_2$ lateral heterostructures by tensile strain.[21] Dai's group calculated the charge transfer and built-in electric field in the in-plane MoS$_2$/WS$_2$ heterostructure,[22] and investigated the straintronics in lateral MoS$_2$/MoSe$_2$ and MoS$_2$/WSe$_2$ heterostructures.[23] Recently, they proposed that lateral heterostructures of WS$_2$ and WSe$_2$ are promising topological insulators.[24] Ozcelik et al. presented a comprehensive study of band alignments of various possible combinations of lateral monolayer heterostructures, including elemental group IV and group V, group III–V compounds, TMD, transition metal trichalcogenides.[25] Lin et al. proposed a novel lateral 2D heterostructure formed by bilayer and monolayer phosphorene and predicted a size-dependent transition between type I and type II band alignment.[26] Very recently, our group explored the electronic properties of 2D S/S heterostructures by taking MoS$_2$/WS$_2$ as a representative, and demonstrated that the intrinsic band alignment of 2D S/S heterostructures should converge slowly to the Anderson limit as the system size increases due to decay of the dipole-induced electrostatic field.[27] This is fundamentally different from the 3D heterostructures where the interfacial condition plays a significant role.

The success of TMD-based lateral 2D heterostructures brings on various new phenomena and calls for novel heterostructures in addition to TMD layers. Monolayer group-IV monochalcogenides with phosphorene-like structures,[28] including GeS, GeSe, SnS and SnSe with compatible lattice parameters,[29] are ideal candidates for forming in-plane heterostructures. These monolayer group-IV monochalcogenides with a suitable bandgap of 1.44–2.32 eV[30–33] have attracted wide attention. Less toxic and earth-abundant GeS, GeSe, SnS and SnSe prepared nanosheets with a thickness down to 1 nm have been explored in the laboratory,[30,31,34–36] and most of them were found to show excellent photoresponse and short photoresponse time with bandgap matching the ideal energy for maximum absorption of incident solar radiation.[37–39] Theoretical calculations predicted that the bandgap of these layered materials increases with decreasing number of layers,[29] but linearly decreases under in-plane compressive strain.[40,41] Moreover, Yan et al. calculated the phonon transport properties and found that these group IV–VI compounds possess diverse anisotropic properties in numerous aspects, such as phonon group velocity, Young's modulus and thermal conductivity.[42] Very recently, our group demonstrated that monolayer group-IV monochalcogenides have superior oxidation resistance as compared to phosphorene.[43] With all these merits, these monolayer materials hold great

promise in several fields, such as photovoltaic cells,[32] anode materials for the lithium ion,[44] thermoelectric devices,[45] and ferroelectric excitonic photovoltaics.[46]

In this study, we propose four types of lateral 2D heterostructures made up of monolayer or multilayer group-IV monochalcogenides: GeS/GeSe, SnS/GeSe, SnSe/GeS and GeS/SnS. Our DFT calculations show that these lateral 2D heterostructures are thermodynamically stable and retain semiconducting behavior. Among them, some heterojunctions possess type II band alignment, permitting potential applications in the high-efficiency solar cell.

Computational methods

All first-principles calculations were carried out using the Vienna Ab initio Simulation Package (VASP)[47] based on DFT with a plane-wave basis set. To treat the exchange–correlation interaction of electrons, we chose the Perdew–Burke–Ernzerhof (PBE) functional[48] within the generalized gradient approximation (GGA). The electron–ion interactions were described by the projector augmented wave (PAW) potentials.[49] The energy cutoff for the plane-wave basis was chosen as 500 eV, and the Brillouin zones (BZ) were sampled by k grids with a uniform spacing of $2\pi \times 0.02$ Å^{-1}. A convergence criterion of 10^{-4} eV for total energy and 0.01 eV Å^{-1} for force were adopted for self-consistent calculation and geometry optimization, respectively. To avoid the interaction between adjacent layers, a vacuum spacing of 20 Å was added along the direction perpendicular to the 2D sheet. Based on the equilibrium structures from PBE calculations, a Heyd–Scuseri–Ernzerhof (HSE06) hybrid functional[50] was used to obtain more accurate band structure for each monolayer, bilayer and trilayer group-IV monochalcogenide.

Results and discussion

We start from the atomic structure and electronic properties of each monolayer group-IV monochalcogenide. Their unit cell structure and 2D BZ are displayed in Fig. 1, and the equilibrium 2D lattice parameters are summarized in Table 1. The electronic
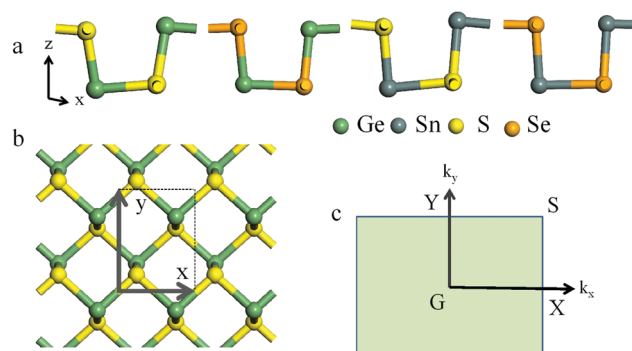

Fig. 1 Atomic structures of (a) four monolayer group-IV monochalcogenides. (b) Top view of GeS monolayer with unit cell specified by arrows and dashed lines. (c) The corresponding 2D Brillouin zone with high-symmetry points: G, X, S and Y.

This journal is © The Royal Society of Chemistry 2017

J. Mater. Chem. C, 2017, **5**, 3788–3795 | **3789**

band structures from both PBE and HSE06 calculations are shown in Fig. S1 of ESI.† For all these monolayers, the dispersions at the valence-band maximum (VBM) are along the Y–G direction, which is in agreement with previous studies.[29,51] As indirect semiconductors, GeS, SnS and SnSe monolayers share similar conduction band dispersion with the conduction-band maximum (CBM) along the G–X direction. On the other hand, the GeSe system with CBM located along the Y–G direction is a direct semiconductor. Analysis of the total density of states (DOS) and partial DOS (Fig. S2, ESI†) for the four monolayer group-IV monochalcogenides further reveals that the VBM is mainly contributed by p states of S and Se, while the CBMs are dominated by p states of Ge and Sn.

The bandgaps obtained from PBE calculations are 1.65, 1.15, 1.46 and 0.88 eV for GeS, GeSe, SnS and SnSe monolayers, respectively. Band structure calculations using a more accurate HSE06 functional yield the same dispersions as PBE, but larger bandgaps of 2.36, 1.74, 2.36 and 1.51 eV for GeS, GeSe, SnS and SnSe, respectively. We further calculated the electron affinity χ and the ionization energy I of each monolayer group-IV monochalcogenide by comparing CBM and VBM with the electrostatic potential level of vacuum, i.e. $\chi = e\phi_{vac} - E_{CBM}$ and $I = e\phi_{vac} - E_{VBM}$. As listed in Table 1, PBE and HSE06 results show a consistent trend, that is, GeS has the largest I, and GeSe has the largest χ.

Starting from the individual monolayer group-IV monochalcogenides as components, we constructed lateral heterostructures with acceptable mismatch (listed in Table 2 and Fig. S1, ESI†). To this end, four monolayer heterostructures (GeS/GeSe, SnS/GeSe, SnSe/GeS and GeS/SnS) can be obtained by stitching two semi-infinite monolayers within the same plane. Because of the smaller mismatch with regard to the armchair orientation (see Table S1, ESI†), the 1D interfaces of these four systems are all along the armchair orientation, as depicted in Fig. 2a. We adopted a parameter n to describe the width of a lateral heterostructure described by a supercell model, that is, a n/n supercell means

n units of group-IV monochalcogenide in both the left and right domains of the heterostructure.

By taking the 8/8 supercell for each monolayer heterostructure as representative, the plane-averaged electron density difference along the direction perpendicular to the 1D boundary and the charge density difference of the interface region are plotted in Fig. 2b–e to illustrate the bonding feature and charge transfer at the interface. As seen from the plane-averaged electron density difference, charge redistribution mainly involves the atoms near the 1D interface. A quantitative analysis shows that the electron redistributions at the interface region ($\Delta\rho > 0.01$ m e Å^{-1}) occur in the width ranges of 10.76, 9.32, 10.90, and 10.38 Å for monolayer GeS/GeSe, SnS/GeSe, SnSe/GeS and GeS/SnS heterostructures, respectively. However, the net electron transfer from one side to another side is tiny, i.e., 2.66, 7.74, 7.61, 6.39 $\times$ 10^{-3} |e| per supercell for monolayers GeS/GeSe, SnS/GeSe, SnSe/GeS, GeS/SnS, respectively. Moreover, as presented in Fig. 2, the two component group-IV monochalcogenide domains in the heterostructure are connected by covalent bonds at the interface, which are slightly weaker than those in the isolated monolayers (shown in Fig. S3 (ESI†) for comparison). As a result, the stability and epitaxial quality of heterostructures would benefit a lot from such seamless and covalent bonds.

The thermodynamic stability of these monolayer heterostructures can be characterized by heat of formation (H_F) defined as the energy cost per area of the supercell:

$$H_F = (E_H - N_L E_L - N_R E_R)/W \times L_H$$

Herein, E_H is the total energy of the heterostructure; N and E with subscripts of L and R (L and R stand for left and right sides of the heterostructure, respectively) are the number of unit cells and the energy of the left and right component materials in one unit cell, respectively; L_H is the periodic length along the 1D interface; W is the width of the supercell, which is perpendicular to the interface. As shown in Fig. S4 (ESI†), all H_F are very small, i.e., on an order of magnitude of about 0.5 eV Å^{-2}. For each system, H_F decreases with the width of the supercell. This can be understood by the fact that a large supercell contributes to the release of strain induced by the lattice mismatch, resulting in lower system energy. Specifically, the strain along the zigzag direction is released with the increase in width. Among the four systems, monolayers GeS/SnS and SnS/GeSe possess relatively lower H_F. This is because stronger Ge–S and Sn–S chemical bonds (see Fig. S3, ESI†) are formed when the GeS/SnS heterostructure is formed, while the SnS/GeSe heterostructure has an extremely small lattice mismatch (see Table S1, ESI†). Nevertheless, the small formation energies ensure that all these heterostructures can be synthesized easily by chemical vapor deposition, which has been demonstrated to be a feasible method to fabricate other lateral 2D heterostructures.[7–9,52,53]

Based on the equilibrium structures of these monolayer heterostructures, we now discuss their electronic properties. The electronic band structures of monolayer heterostructures modeled by the 8/8 supercell from PBE calculations are shown in Fig. 3. Clearly, after being stitched into one monolayer within the same plane, all these group-IV monochalcogenide heterostructures

Table 1 Fundamental structural and electronic properties of monolayer group-IV monochalcogenides: lattice parameters (a, b) calculated with the PBE method; bandgap (E_g), electron affinity (χ) and ionization energy (I) calculated with PBE and HSE06 methods

	a (Å)	b (Å)	E_g (eV)		χ (eV)		I (eV)	
			PBE	HSE06	PBE	HSE06	PBE	HSE06
GeS	3.68	4.40	1.65	2.36	3.35	2.97	5.00	5.33
GeSe	3.99	4.26	1.15	1.74	3.42	3.16	4.57	4.90
SnS	4.09	4.26	1.46	2.11	3.15	2.87	4.61	4.98
SnSe	4.27	4.41	0.88	1.51	3.42	3.13	4.30	4.64

Table 2 The mismatch defined by $|(a_1 - a_2)|/a_m|$, where a_1 is the lattice constant of one domain, a_2 is the lattice constant of another domain, and a_m is the maximum value of a_1 and a_2. H_F is the heat of formation for a heterostructure with an 8/8 supercell of ~65 Å width in the x direction

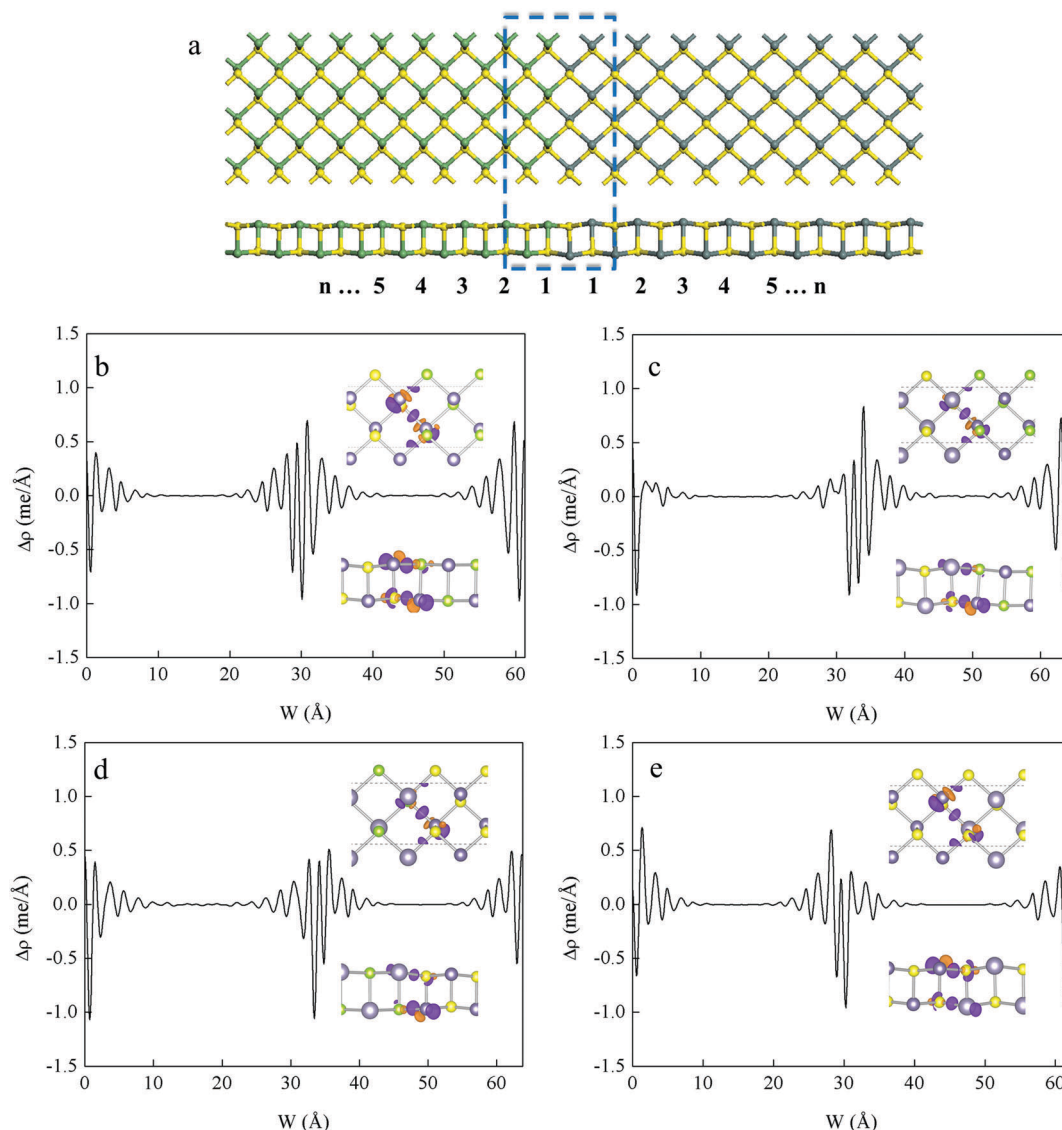|	GeS/GeSe	SnS/GeSe	SnSe/GeS	GeS/SnS
Mismatch	3.18%	<0.001%	0.2%	3.18%
H_F (eV Å^{-2})	0.29	0.23	0.43	0.21

Fig. 2 Atomic configurations of (a) monolayer GeS/SnS with armchair interface, the yellow balls are S atoms, the green balls are Ge atoms, and the blue balls are Sn atoms. Plane-averaged electron density difference along the direction perpendicular to the 1D interface for monolayer (b) GeS/GeSe, (c) SnS/GeSe, (d) SnSe/GeS and (e) GeS-SnS. The insets are the charge density difference for the interface region of heterostructures highlighted by the blue dashed line in (a): the lower plot for side view and the upper plot for top view. The purple and orange areas represent electron accumulation and depletion, respectively (isosurface value = 0.007 e Å^{-3}).

retain semiconducting behavior well, and there is no edge state or mid-gap state. Similar to most isolated systems, the CBM is located along the $G–X$ direction with slightly smaller indirect bandgaps of 1.35, 1.07, 1.21, and 1.54 eV for monolayers GeS/GeSe, SnS/GeSe, SnSe/GeS and GeS/SnS, respectively. The VBM is located along the $X–S$ direction for monolayer GeSe/GeS and SnSe/GeS systems and the $Y–G$ direction for monolayer SnS/GeSe and GeS/SnS ones.

Furthermore, the partial charge densities for the VBM and VBM states of monolayer GeS/GeSe and GeS/SnS heterostructures are calculated and presented in Fig. 3e and f. For monolayer GeS/GeSe heterostructure, the CBM (VBM) state distributes on the Ge (Se) atoms in the central region of the GeSe domain. In contrast, the CBM state of the monolayer GeS/SnS heterostructure is mainly

contributed by the Sn atoms in the central region of the SnS domain, while the CBM states distribute on the S atoms near the interface from both sides. The partial charge density of VBM and CBM states for monolayer SnS/GeSe and SnSe/GeS systems are shown in Fig. S6 (ESI†). Analogous to monolayer GeS/GeSe, the VBM and CBM states of monolayer SnSe/GeS heterostructure were mainly distributed on Se and Ge atoms in the central region of the GeSe side, respectively. Moreover, the situation of monolayer SnS/GeSe is similar to that of monolayer GeS/SnS, with VBM being contributed by Se atoms in the central GeSe region, as well as CBM being dominated by the Ge atoms along with little contribution by the Sn and S atoms near the interface.

Previous theoretical studies have revealed that the electronic properties of a 2D lateral heterostructure may depend on the
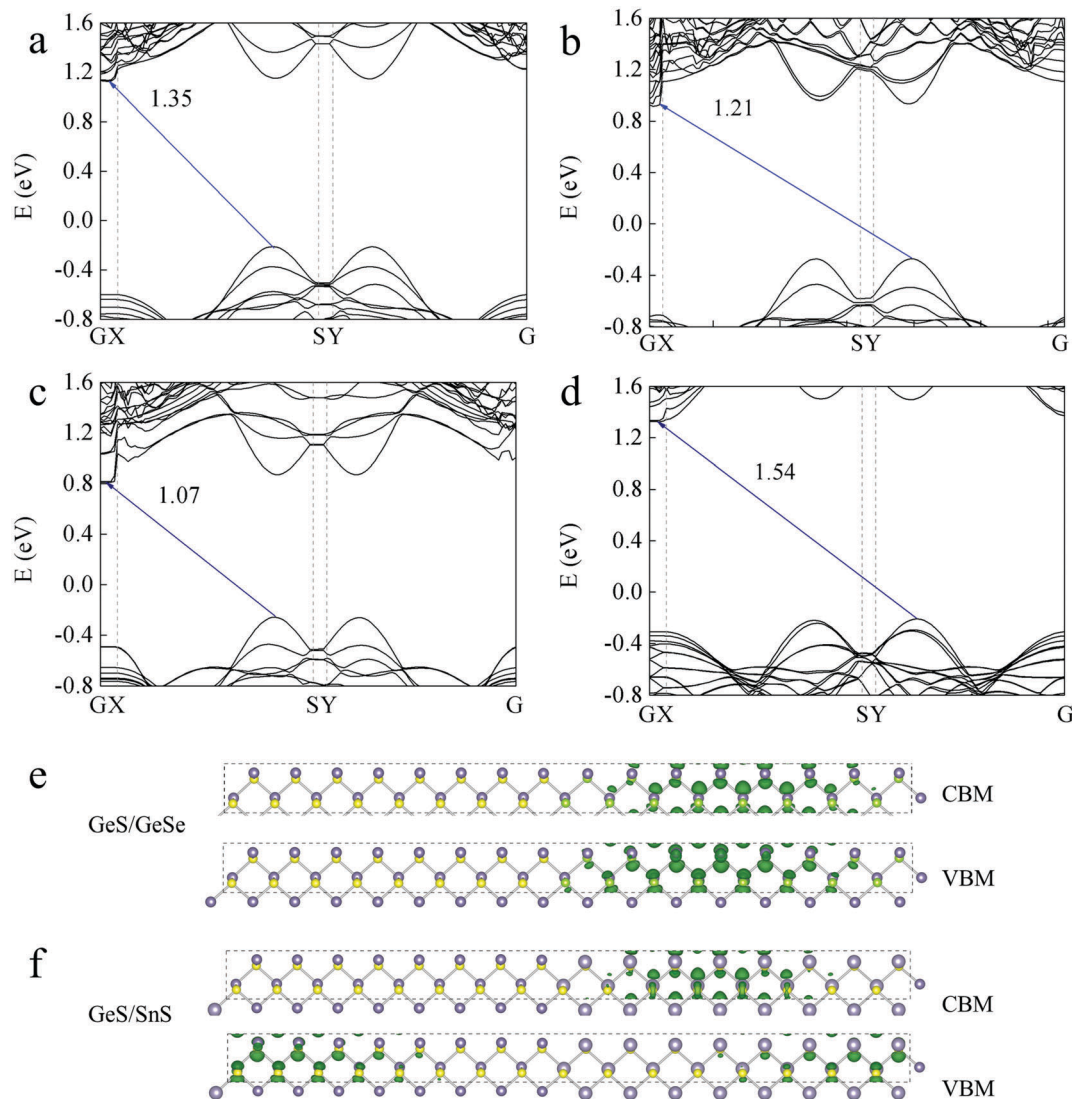
Fig. 3 Band structures for monolayer (a) GeS/GeSe, (b) SnS/GeSe, (c) SnSe/GeS, and (d) GeS/SnS heterostructures from PBE calculations. The partial charge distributions corresponding to the VBM and CBM for monolayer (e) GeS/GeSe and (f) GeS/SnS heterostructures. The bandgap for each system (in units of eV) is labeled by a blue arrow.

supercell size.[27,54,55] To gain insight into the size dependence of the current systems, we reduced the domain width of the monolayer heterostructure supercell from $n = 8$ to $n = 3$, as schematically shown in Fig. 2a. In the largest 8/8 case, the supercell sizes are 61.32, 64.57, 63.64 and 62.15 Å for GeS/GeSe, SnS/GeSe, SnSe/GeS and GeS/SnS, respectively, which are much larger than the range of electron redistribution shown in Fig. 2b to e. As seen in Fig. 4, bandgaps of the four monolayer heterostructures decrease gradually with increasing supercell widths. A similar phenomenon was found in other lateral heterostructures.[26,54,56] Within the supercell model, when a heterostructure has a small width, it can be viewed as a periodic superlattice in which the quantum confinement effect plays an important role in determining the intrinsic electronic properties of each domain. With increasing width, the quantum confinement effect vanishes and every domain gradually reaches the limit of phase separation. On the other hand, the

Coulomb effect due to the accumulated charge near the inter-line (i.e., interfacial dipole) in a lateral 2D heterostructure decays slowly with increasing supercell width. Considering both effects, the bandgap of an S/S heterostructure would converge to the intrinsic bandgap of the component 2D semi-conductor when the size of supercell is large enough. From our supercell calculations, the heterostructure bandgaps were found to be 1.35, 1.21, 1.07 and 1.54 eV for monolayers GeS/GeSe, SnS/GeSe, SnSe/GeS and GeS/SnS, respectively; in addition, their intrinsic bandgaps from individual components should be 1.15, 1.15, 0.88 and 1.26 eV (noting that 1.26 eV for monolayer GeS/SnS is the difference between the CBM of isolated GeS and VBM of isolated SnS), respectively. Undoubtedly, the bandgaps determined from these two methods share the same sequence, which is SnSe/GeS > SnS/GeSe ≥ GeS/GeSe > GeS/SnS. The difference between these two types of band gaps up to about 0.3 eV originates from both finite confinement
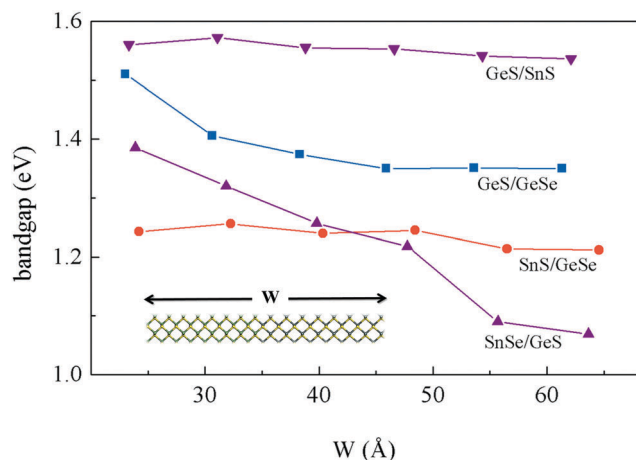
Fig. 4 Dependence of bandgap on supercell width W of four monolayer heterostructures. The inset shows the atomic structure of the supercell model.

effect of each semiconductor domain and electrostatic potential due to interfacial dipole, which has been discussed in detail in our recent study.[27]

It is also noteworthy that monolayer SnS/GeSe heterostructure has an indirect bandgap. However, as we will discuss later, the GeS/GeSe system exhibits type I band alignment, which should share the same character (direct or indirect) of the narrow bandgap semiconductor, i.e., GeSe with a direct bandgap. In order to explain this inconsistency, we compared the direct and indirect bandgap of SnSe/GeS with different widths (i.e., 5/5, 6/6, 7/7 and 8/8 supercells). Due to the quantum confinement effect, all these heterostructures have indirect bandgaps, and the difference (ΔE) between direct bandgap and indirect bandgap of each heterostructure reduces with increasing width, i.e., $\Delta E = 0.088$ eV, 0.065 eV, 0.033 eV and 0.022 eV for 5/5, 6/6, 7/7 and 8/8 supercells, respectively, as shown in Fig. S5 (ESI†). Hence, when the width of a GeS/GeSe heterostructure is large enough, it would eventually converge to a direct bandgap system.

The band alignments, i.e. the conduction band offset (CBO) and valence band offset (VBO), are key parameters in determining the electrical and optical properties of an S/S heterostructure, which have a significant effect on the transport properties of the carriers at the interface. An S/S junction with type I band alignment consists of two semiconductors, wherein one semiconductor has a higher (lower) VBM and a lower (higher) CBM with respect to the other one; moreover, both the VBM and CBM of one component stay in the lower (higher) energy level than the corresponding band edges of the other component in a type II S/S junction. Using the electrostatic potential level in vacuum as reference energy for each isolated monolayer group-IV monochalcogenide, the calculated VBO and CBO of four monolayer heterostructures at Anderson limits[57] are presented in Fig. 5 and Table S2 (ESI†). The PBE and HSE06 calculations give nearly identical VBO values with deviation less than 0.04 eV, while the largest difference of CBO values between PBE and HSE06 methods reaches 0.11 eV. More importantly, the band alignments at the Anderson limit reveal that the monolayer GeS/SnS heterostructures have the characters of type II band alignment, while the other three monolayer heterostructures belong to type I alignment, as shown in Fig. 4. Furthermore, we calculated the band offsets using the local DOS with 9/9 supercells for all four monolayer heterostructures,[26] and the results show the same alignment types, as shown in Fig. S7 (ESI†). Since the experimentally synthesized group-IV monochalcogenides are usually multilayer,[58–60] it is important to investigate the band alignments of multilayer heterostructures. The calculated band-edge positions relative to the vacuum energy of bilayer and trilayer systems are presented in Fig. S8 (ESI†), which show that the band alignments of bilayer and trilayer heterostructures at the Anderson limit are somehow different from that of the monolayer. For the bilayer and trilayer heterostructures, GeS/SnS retains type II band alignment, while GeS/GeSe and GeS/SnSe retain type I band alignment. However, increasing the number of layers changes the band alignment of the SnS/GeSe heterostructure from type I to Type II. The CBO and VBO of monolayer, bilayer and trilayer SnS/GeSe heterostructures are shown in Fig. S9 (ESI†).
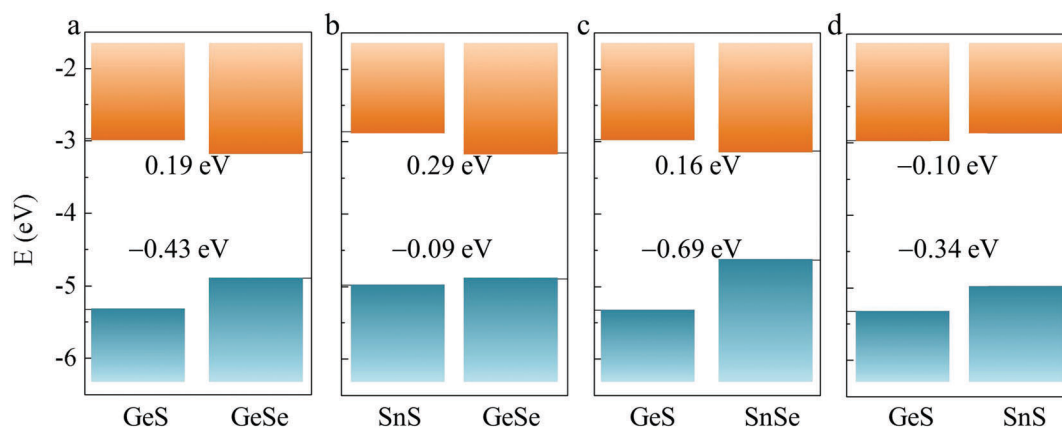

Fig. 5 Band alignments of monolayer (a) GeS/GeSe, (b) SnS/GeSe, (c) SnSe/GeS and (d) GeS/SnS at the Anderson limit calculated with the HSE06 method. In each plot, the orange (upper) is for the conduction band and the blue (lower) is for the valence band; the upper number is the conduction band offset (CBO), and the lower number is the valence band offset (VBO). The vacuum level is set to zero energy.

Two types of band alignments exist in these lateral hetero-structures, making these heterogeneous materials promising candidates for future optoelectronic devices.[25,61] In the mono-layer/multilayer GeS/SnS heterostructures and multilayer SnS/GeSe heterostructures with type II band alignment, both CBM and VBM of one domain are lower than those of the other one, suggesting possible photovoltaic applications. This heterostructure-based solar cell may permit high efficiency with two possible reasons: (1) it has suitable bandgap compatible with visible light (1.54 eV from the 8/8 supercell calculation and 1.26 eV at the Anderson limit for monolayer GeS/SnS; 1.482 and 1.363 eV at the Anderson limit for bilayer and trilayer SnS/GeSe, respectively); thus these heterostructures can capture a wider range of sunlight to produce excitons, reducing the energy loss. (2) Another advantage is that in the heterostructure with type II band alignment, once the exciton is produced in one domain, either the electron or the hole will be transferred through the interface, permitting the photo-electric conversion.[61] Moreover, the excited carriers of this type of alignment have longer lifetimes,[13,61] which is desirable in photovoltaics. Moreover, both the building components possess diverse anisotropic properties, thus proving this heterostructure to be advantageous for directional charge transport. Other hetero-structures with a type I band alignment also hold promise for light emitting diodes[62,63] and lasers.[25,64] Specifically, these heterostruc-tures may find applications in a solar concentrator[65] due to the suitable bandgaps of these monolayer or multilayer group-IV monochalcogenides matching those of visible sunlight. Compared with traditional 3D materials, these 2D materials with a large surface-to-volume ratio should have improved light absorption. In fact, several low-dimensional materials and nanostructures[66-68] have been reported to possess high efficiency in optoelectronic devices. Our theoretical study has offered several potential candi-date materials for future electronics and optoelectronics.

Conclusions

In summary, we propose novel lateral 2D heterostructures based on monolayer group-IV monochalcogenides as compo-nents, with 1D interfaces along the armchair orientation. Using first-principles calculations, we investigated the structural properties and thermodynamic stability of monolayer hetero-structures. The results show that two component domains are spliced with covalent bonds and should be easily synthesized in a laboratory using chemical vapor deposition. We also explored the electronic properties of monolayer heterostructures and found that the semiconducting behavior is retained in these hetero-structures. Moreover, the bandgap decreases with the increasing width of the supercell. The band alignments of monolayer, bilayer and trilayer heterostructures at the Anderson limit have been calculated. The results show that some heterostructures belong to type II band alignment and are promising candidate materials for solar cells with high efficiency. As an extension of the current study, it is possible to combine monolayer (or multilayer) GeS and SnSe with monolayer (or multilayer) phosphorene to form in-plane heterostructures with mismatches of 4.41%

and 4.19%, respectively. The combination of the polar group-IV monochalcogenides and nonpolar phosphorene is expected to result in many fascinating phenomena in these heterostructures.

Acknowledgements

References

1 Q. H. Wang, K. Kalantar-Zadeh, A. Kis, J. N. Coleman and M. S. Strano, *Nat. Nanotechnol.*, 2012, **7**, 699–712.

2 J. Zhao, H. Liu, Z. Yu, R. Quhe, S. Zhou, Y. Wang, C. C. Liu, H. Zhong, N. Han, J. Lu, Y. Yao and K. Wu, *Prog. Mater. Sci.*, 2016, **83**, 151.

3 Y. C. Cheng, Z. Y. Zhu, M. Tahir and U. Schwingenschlogl, *EPL*, 2013, **102**, 57001.

4 M.-Y. Li, C.-H. Chen, Y. Shi and L.-J. Li, *Mater. Today*, 2016, **19**, 322–335.

5 K. S. Novoselov, A. Mishchenko, A. Carvalho and A. H. Castro Neto, *Science*, 2016, **353**, 461.

6 A. K. Geim and I. V. Grigorieva, *Nature*, 2013, **499**, 419–425.

7 Y. J. Gong, J. H. Lin, X. L. Wang, G. Shi, S. D. Lei, Z. Lin, X. L. Zou, G. L. Ye, R. Vajtai, B. I. Yakobson, H. Terrones, M. Terrones, B. K. Tay, J. Lou, S. T. Pantelides, Z. Liu, W. Zhou and P. M. Ajayan, *Nat. Mater.*, 2014, **13**, 1135–1142.

8 X. Duan, C. Wang, J. C. Shaw, R. Cheng, Y. Chen, H. Li, X. Wu, Y. Tang, Q. Zhang, A. Pan, J. Jiang, R. Yu, Y. Huang and X. Duan, *Nat. Nanotechnol.*, 2014, **9**, 1024–1030.

9 C. Huang, S. Wu, A. M. Sanchez, J. J. P. Peters, R. Beanland, J. S. Ross, P. Rivera, W. Yao, D. H. Cobden and X. Xu, *Nat. Mater.*, 2014, **13**, 1096–1101.

10 M.-Y. Li, Y. Shi, C.-C. Cheng, L.-S. Lu, Y.-C. Lin, H.-L. Tang, M.-L. Tsai, C.-W. Chu, K.-H. Wei, J.-H. He, W.-H. Chang, K. Suenaga and L.-J. Li, *Science*, 2015, **349**, 524–528.

11 J. F. Zhang, W. Y. Xie, X. H. Xu, S. B. Zhang and J. J. Zhao, *Chem. Mater.*, 2016, **28**, 5022–5028.

12 J. Kang, S. Tongay, J. Zhou, J. B. Li and J. Q. Wu, *Appl. Phys. Lett.*, 2013, **102**, 012111.

13 P. Rivera, J. R. Schaibley, A. M. Jones, J. S. Ross, S. Wu, G. Aivazian, P. Klement, K. Seyler, G. Clark, N. J. Ghimire, J. Yan, D. G. Mandrus, W. Yao and X. Xu, *Nat. Commun.*, 2015, **6**, 6242.

14 M.-H. Chiu, C. Zhang, H.-W. Shiu, C.-P. Chuu, C.-H. Chen, C.-Y. S. Chang, C.-H. Chen, M.-Y. Chou, C.-K. Shih and L.-J. Li, *Nat. Commun.*, 2015, **6**, 7666.

15 Y. Son, M. Y. Li, C. C. Cheng, K. H. Wei, P. W. Liu, Q. H. Wang, L. J. Li and M. S. Strano, *Nano Lett.*, 2016, **16**, 3571–3577.

16 C. Zhang, Y. Chen, J.-K. Huang, X. Wu, L.-J. Li, W. Yao, J. Tersoff and C.-K. Shih, *Nat. Commun.*, 2016, **7**, 10346.

17 S. Zhang, Z. Yan, Y. Li, Z. Chen and H. Zeng, *Angew. Chem., Int. Ed.*, 2015, **54**, 3112–3115.

18 Y. Gong, S. Lei, G. Ye, B. Li, Y. He, K. Keyshar, X. Zhang, Q. Wang, J. Lou, Z. Liu, R. Vajtai, W. Zhou and P. M. Ajayan, *Nano Lett.*, 2015, **15**, 6135–6141.

19 J. Chen, W. Zhou, W. Tang, B. Tian, X. Zhao, H. Xu, Y. Liu, D. Geng, S. J. R. Tan, W. Fu and K. P. Loh, *Chem. Mater.*, 2016, **28**, 7194–7197.

20 X.-Q. Zhang, C.-H. Lin, Y.-W. Tseng, K.-H. Huang and Y.-H. Lee, *Nano Lett.*, 2015, **15**, 410–415.

21 J. Kang, H. Sahin and F. M. Peeters, *J. Phys. Chem. C*, 2015, **119**, 9580–9586.

22 W. Wei, Y. Dai and B. B. Huang, *Phys. Chem. Chem. Phys.*, 2016, **18**, 15632–15638.

23 W. Wei, Y. Dai and B. Huang, *Phys. Chem. Chem. Phys.*, 2017, **19**, 663–672.

24 Q. L. Sun, Y. Dai, C. W. Niu, Y. D. Ma, W. Wei, L. Yu and B. B. Huang, *2D Mater.*, 2017, **4**, 025038.

25 V. O. Ozcelik, J. G. Azadani, C. Yang, S. T. Koester and T. Low, *Phys. Rev. B*, 2016, **94**, 035125.

26 H. F. Lin, L. M. Liu and J. J. Zhao, *J. Mater. Chem. C*, 2017, **5**, 2291–2300.

27 J. F. Zhang, W. Y. Xie, J. J. Zhao and S. B. Zhang, *2D Mater.*, 2017, **4**, 015038.

28 G. S. Shi and E. Kioupakis, *Nano Lett.*, 2015, **15**, 6926–6931.

29 L. C. Gomes and A. Carvalho, *Phys. Rev. B: Condens. Matter Mater. Phys.*, 2015, **92**, 085406.

30 S. Zhao, H. Wang, Y. Zhou, L. Liao, Y. Jiang, X. Yang, G. Chen, M. Lin, Y. Wang, H. Peng and Z. Liu, *Nano Res.*, 2015, **8**, 288–295.

31 P. Ramasamy, D. Kwak, D.-H. Lim, H.-S. Ra and J.-S. Lee, *J. Mater. Chem. C*, 2016, **4**, 479–485.

32 X. Liu, Y. Li, B. Zhou, X. Wang, A. N. Cartwright and M. T. Swihart, *Chem. Mater.*, 2014, **26**, 3515–3521.

33 R. K. Ulaganathan, Y.-Y. Lu, C.-J. Kuo, S. R. Tamalampudi, R. Sankar, K. M. Boopathi, A. Anand, K. Yadav, R. J. Mathew, C.-R. Liu, F. C. Chou and Y.-T. Chen, *Nanoscale*, 2016, **8**, 2284–2292.

34 D.-J. Xue, J. Tan, J.-S. Hu, W. Hu, Y.-G. Guo and L.-J. Wan, *Adv. Mater.*, 2012, **24**, 4528–4533.

35 C. Li, L. Huang, G. P. Snigdha, Y. Yu and L. Cao, *ACS Nano*, 2012, **6**, 8868–8877.

36 L. Li, Z. Chen, Y. Hu, X. Wang, T. Zhang, W. Chen and Q. Wang, *J. Am. Chem. Soc.*, 2013, **135**, 1213–1216.

37 L. Li, Z. Chen, Y. Hu, X. W. Wang, T. Zhang, W. Chen and Q. B. Wang, *J. Am. Chem. Soc.*, 2013, **135**, 1213–1216.

38 B. Mukherjee, Y. Q. Cai, H. R. Tan, Y. P. Feng, E. S. Tok and C. H. Sow, *ACS Appl. Mater. Interfaces*, 2013, **5**, 9594–9604.

39 S. L. Zhao, H. A. Wang, Y. Zhou, L. Liao, Y. Jiang, X. Yang, G. C. Chen, M. Lin, Y. Wang, H. L. Peng and Z. F. Liu, *Nano Res.*, 2015, **8**, 288–295.

40 L. Huang, F. G. Wu and J. B. Li, *J. Chem. Phys.*, 2016, **144**, 114708.

41 Y. H. Hu, S. L. Zhang, S. F. Sun, M. Q. Xie, B. Cai and H. B. Zeng, *Appl. Phys. Lett.*, 2015, **107**, 122107.

42 G. Z. Qin, Z. Z. Qin, W. Z. Fang, L. C. Zhang, S. Y. Yue, Q. B. Yan, M. Hu and G. Su, *Nanoscale*, 2016, **8**, 11306–11319.

43 Y. Guo, S. Zhou, Y. Z. Bai and J. J. Zhao, *ACS Appl. Mater. Interfaces*, 2017, DOI: 10.1021/acsami.6b16786.

44 J. Lu, C. Y. Nan, L. H. Li, Q. Peng and Y. D. Li, *Nano Res.*, 2013, **6**, 55–64.

45 L.-D. Zhao, S.-H. Lo, Y. Zhang, H. Sun, G. Tan, C. Uher, C. Wolverton, V. P. Dravid and M. G. Kanatzidis, *Nature*, 2014, **508**, 373.

46 W. Hua and Q. Xiaofeng, *2D Mater.*, 2017, **4**, 015010.

47 G. Kresse and J. Furthmuller, *Phys. Rev. B: Condens. Matter Mater. Phys.*, 1996, **54**, 11169–11186.

48 J. P. Perdew, K. Burke and M. Ernzerhof, *Phys. Rev. Lett.*, 1997, **78**, 1396.

49 G. Kresse and D. Joubert, *Phys. Rev. B: Condens. Matter Mater. Phys.*, 1999, **59**, 1758–1775.

50 A. V. Krukau, O. A. Vydrov, A. F. Izmaylov and G. E. Scuseria, *J. Chem. Phys.*, 2006, **125**, 224106.

51 G. Shi and E. Kioupakis, *Nano Lett.*, 2015, **15**, 6926–6931.

52 C. Tan and H. Zhang, *J. Am. Chem. Soc.*, 2015, **137**, 12162–12174.

53 S. Najmaei, Z. Liu, W. Zhou, X. Zou, G. Shi, S. Lei, B. I. Yakobson, J.-C. Idrobo, P. M. Ajayan and J. Lou, *Nat. Mater.*, 2013, **12**, 754–759.

54 Q. Sun, Y. Dai, Y. Ma, N. Yin, W. Wei, L. Yu and B. Huang, *2D Mater.*, 2016, **3**, 035017.

55 O. Leenaerts, S. Vercauteren, B. Schoeters and B. Partoens, *2D Mater.*, 2016, **3**, 025012.

56 W. Wei, Y. Dai, C. Niu and B. Huang, *Sci. Rep.*, 2015, **5**, 17578.

57 R. L. Anderson, *Solid-State Electron.*, 1962, **5**, 341.

58 P. Ramasamy, D. Kwak, D. H. Lim, H. S. Ra and J. S. Lee, *J. Mater. Chem. C*, 2016, **4**, 479–485.

59 D. J. Xue, J. H. Tan, J. S. Hu, W. P. Hu, Y. G. Guo and L. J. Wan, *Adv. Mater.*, 2012, **24**, 4528–4533.

60 D. D. Vaughn II, S. In and R. E. Schaak, *ACS Nano*, 2011, **5**, 8852–8860.

61 S. S. Lo, T. Mirkovic, C.-H. Chuang, C. Burda and G. D. Scholes, *Adv. Mater.*, 2011, **23**, 180–197.

62 F. Withers, O. Del Pozo-Zamudio, A. Mishchenko, A. P. Rooney, A. Gholinia, K. Watanabe, T. Taniguchi, S. J. Haigh, A. K. Geim, A. I. Tartakovskii and K. S. Novoselov, *Nat. Mater.*, 2015, **14**, 301–306.

63 S. Nakamura, N. Senoh, N. Iwasa and S. I. Nagahama, *Jpn. J. Appl. Phys.*, 1995, **34**, L797–L799.

64 Y. Arakawa and A. Yariv, *IEEE J. Quantum Electron.*, 1986, **22**, 1887–1899.

65 L. R. Bradshaw, K. E. Knowles, S. McDowall and D. R. Gamelin, *Nano Lett.*, 2015, **15**, 1315–1323.

66 F. Priolo, T. Gregorkiewicz, M. Galli and T. F. Krauss, *Nat. Nanotechnol.*, 2014, **9**, 19–32.

67 R. Yu, Q. Lin, S.-F. Leung and Z. Fan, *Nano Energy*, 2012, **1**, 57–72.

68 J. Zhu, Z. Yu, G. F. Burkhard, C.-M. Hsu, S. T. Connor, Y. Xu, Q. Wang, M. McGehee, S. Fan and Y. Cui, *Nano Lett.*, 2009, **9**, 279–282.